Design and Evaluation of Feedforward Active Ripple Filters

Mingjuan Zhu, David J. Perreault, *Member, IEEE*, Vahe Caliskan, Timothy C. Neugebauer, Stephan Guttowski, and John G. Kassakian, *Fellow, IEEE*

***Abstract*—An active ripple filter is an electronic circuit that cancels or suppresses the ripple current and electromagnetic interference generated by the power stage of a power converter, thus reducing the passive filtration requirements. This paper explores the design of feedforward active ripple filters for current ripple cancellation, including the design tradeoffs, advantages, and limitations of different implementation methods. The design and performance of an active filter using a novel Rogowski-coil current sensor is discussed in detail. Experimental results from a prototype converter system using this approach are presented, and quantitative comparisons are made between a hybrid passive/active filter and a purely passive filter. It is demonstrated that substantial improvements in filter mass and converter transient performance are achievable using this active ripple filtering method.**

***Index Terms*—Active ripple filter, electromagnetic interference (EMI), hybrid passive/active filter, Rogowski-coil current sensor.**

I. Introduction

INPUT and output filters have become an extremely important part of modern switching power converters, and often account for a substantial portion of converter size and cost. Traditionally, passive LC low-pass filters have been employed to attenuate power converter switching ripple to acceptable levels [1]–[3]. However, the tight ripple specifications that are often imposed for application reasons or to meet conducted electromagnetic interference (EMI) specifications can result in bulky and expensive filters that are detrimental to the transient performance of the system. This is especially true for systems that operate at high current levels, due to the nature of the filter components and their parasitics.

An alternative to the conventional approach is the use of an active ripple filter, in which an active electronic circuit (typically coupled with a reduced passive filter) is used to cancel or suppress ripple components at the filter output [4]–[13]. Typically, the reduced passive filter attenuates the ripple to an intermediate level at which the active electronics can cancel or suppress the ripple to an even lower level without undue power loss. For example, Fig. 1 shows a feedforward active ripple filter used in conjunction with a passive filter at the output of a buck converter. The active filter senses the ripple current in the passive filter inductance and shunts an exact copy of it away from the output capacitance and load. This reduces the ripple seen at the output, and permits a substantially smaller passive filter to be employed than would otherwise be possible. Potential benefits of the active filter approach thus include reduction of the converter size and cost, and improvements in transient performance.

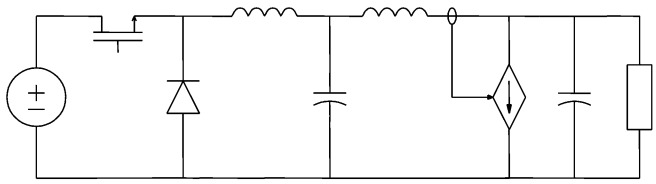

Fig. 1. Feedforward current-ripple active filter used in conjunction with a passive filter on the output of a buck converter. The active filter allows a much smaller passive filter to be employed.

Many types of active ripple filters are possible. Ripple-current filters (such as the one illustrated in Fig. 1) reduce the ripple current passing through a circuit branch [6]–[12], while ripple-voltage filters reduce the voltage ripple at a node [4]–[6], [13]. Feedforward filters achieve the ripple reduction by measuring a ripple component and injecting its inverse [4], [8]–[10], [13], while feedback filters operate to suppress the ripple via high-gain feedback control [4]–[7], [9]–[13]. Hybrids of these filter types are also possible (see [4], [9], [13], for example), and active filters may be further classified by how the sensing and driving functions are implemented [6].

This paper explores the design of feedforward ripple-current active filters. Design of both the current sensor and current injector elements of these filters is considered, and the advantages, limitations, and design tradeoffs of different implementation methods are addressed. The design and experimental evaluation of an active ripple filter using a novel Rogowski-coil current sensor is treated in detail. Section II of the paper considers the design of current sensors for active ripple filters, including the Rogowski-coil sensor. The design of two different types of current injectors is addressed in Section III. Section IV describes the application of the active filter technique to the output filter of a power converter. Active filter elements of the designs developed in Sections II and III are coupled with a small passive filter to form a hybrid passive/active output filter. The paper presents experimental results from the prototype converter system, and compares the hybrid passive/active filter to an entirely passive filter meeting the same ripple attenuation specification. Finally,

Manuscript received August 13, 2002; revised September 8, 2004. This work was supported by the United States Office of Naval Research under Grants N00014-96-1-0524 and N00014-00-1-0381, and by the member companies of the MIT/Industry Consortium on Advanced Automotive Electrical/Electronic Components and Systems. Recommended by Associate Editor P. Mattavelli.

M. Zhu is with Remec, Inc., San Diego, CA 92123 USA.

D. J. Perreault and J. G. Kassakian are with the Laboratory for Electromagnetic and Electronic Systems, Massachusetts Institute of Technology, Cambridge, MA 02139 USA (e-mail: djperrea@mit.edu).

V. Caliskan is with the Automotive Communications and Electronic Systems Group, Motorola, Inc., Palatine, IL 60067 USA.

T. C. Neugebauer is with Draper Laboratories, Boston, MA 02108 USA.

S. Guttowski is with the Fraunhofer Institute for Microintegration and Reliability (IZM), Berlin 13355, Germany.

Digital Object Identifier 10.1109/TPEL.2004.843018

Section V draws conclusions and presents an evaluation of the feedforward ripple-current active filtering approach.

II. Current Sensing

Successful implementation of a feedforward current-ripple cancellation scheme (such as illustrated in Fig. 1) requires that the ripple current be both sensed and replicated with great fidelity. Therefore, the current sensor and injector must each have wide bandwidth, an accurately known gain with low sensitivity to parameter variations, and low phase shift[1]. The current sensor must also be able to tolerate (and reject) the large dc (power frequency) component of the current.

A. Inductor-Voltage-Based Sensor

One approach that has been used to sense ripple current for active filtering is integrating the voltage across a converter or filter inductor, either directly or through the use of a second sense winding [8], [10]. While the approach is very inexpensive, it is also problematic because the sensor gain depends directly on inductance (which can vary across different units, time, temperature, and flux levels), though this limitation can be partially mitigated through the use of adaptive tuning methods [8]. This method is also sensitive to other inductor nonidealities such as equivalent series resistance. We will not further address this sensor type here.

B. Current Transformer Sensor

Current transformers have also been employed for current ripple sensing in active filters [9], [11]. While this approach can yield isolated, high bandwidth measurements, the current transformer must be designed so that it does not saturate while carrying the dc component of the primary current, which increases its size and cost. Here we consider the design of current-transformer-based sensors for active ripple filtering applications.

Fig. 2 shows a complete current transformer sensor, including the current transformer (CT), a burden resistor, and an amplifier. The parasitic elements of the CT are also illustrated: the leakage inductances L_{l1} and L_{l2} arise from the fact that all of the flux from the primary winding does not link the secondary winding and vice versa, while the magnetizing inductance term L_μ arises from the fact that the permeability of the core is finite. To understand the operation of the CT sensor, neglect the parasitics. When a current i_1 flows in the primary winding, a proportional current is induced in the secondary winding. This current passes through the burden resistor, whose voltage is subsequently amplified by the amplifier, generating an output voltage that is ideally proportional to the primary current. The turns ratio $N_1 \mu N_2$ is generally made small so that the secondary current is much smaller than the sensed current, and so that the burden impedance reflected to the primary is small.

The major design constraints of the CT sensor result from the parasitics of the transformer. The magnetizing inductance needs to be large enough so that the ripple current is sensed accurately with low phase shift. If the amplifier dynamics and secondary-side leakage inductance L_{l2} are neglected, then the

[1]For small errors, the fractional residual ripple due to a gain error is approximately equal to the fractional gain error, and the fractional residual ripple due to a phase error is approximately equal to the phase error (measured in radians). Hence, either a 10% magnitude error or a 5.7° (0.1 radian) phase error results in 10% residual ripple.

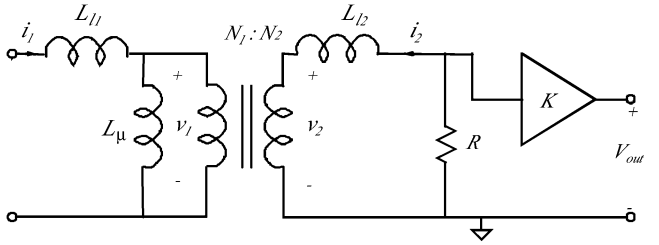

Fig. 2. Current sensor based on a current transformer, including a current transformer (CT), a burden resistor, and an amplifier. Parasitics of the current transformer are also illustrated.

transfer function from the sensor input current i_1 to output voltage v_o can be written as

$$\frac{v_{\text{out}}}{i_1} = \frac{N_1}{N_2} RK \left[\frac{s}{s + \frac{N_2^2 R}{N_2^2 L_\mu}} \right] \tag{1}$$

The high-pass nature of this transfer function reflects the fact that at low frequencies (including dc), the current i_1 will not induce a current through the burden resistor (and thus result in an output voltage), but will instead serve to magnetize the core (i.e., will be shunted through the magnetizing inductance in the model of Fig. 2). To achieve low phase shift, the pole in (1) needs to be at least a decade below the lowest ripple frequency of interest, which sets a lower limit on the allowable magnetizing inductance for a given turns ratio and burden resistance. Furthermore, the large dc component of the current (carried by the magnetizing inductance) must not saturate the core. Together, these constraints determine the energy storage requirement of the transformer and hence the size of the core. Based on these constraints, the required core volume, V_c, can easily be shown to be

$$V_c = \frac{\mu_c L_\mu I_p^2}{B_{\text{sat}}^2} \tag{2}$$

where μ_c is the permeability of the core, L_μ is the magnetizing inductance, I_p is the peak value of the sensed current, and B_{sat} is the maximum allowed flux density in the core.

From (2), we can see that the required volume of the core can be reduced by making L_μ smaller. As seen in (1), however, reduction of L_μ requires a commensurate reduction in R to maintain a small phase shift. Reduction in R in turn necessitates an increase in amplifier gain to maintain a constant current sensing gain. Furthermore, if R is made too small then the voltage drop across the secondary-side leakage inductance becomes significant, and error in introduced in the amplitude and phase of the sensed signal. Ultimately, the minimum size of the core is limited by the amplification requirements along with the effects of transformer leakage inductance.

Here, we carry out the design of current transformers for a given ripple current specification but different dc current levels in order to illustrate the practical result of (2). The sensors are designed for an ac ripple current magnitude of 100 mA with a fundamental frequency on the order of 100 kHz, with a sensor gain of 10 V/A. Sensor design for dc current levels of 1 A to 50 A are considered. The design parameters common to all of the sensors are illustrated in Table I. A primary to secondary turns ratio of 1:100 is chosen along with a burden resistance of 10 Ω; this gives a reflected resistance of 1 mΩ on the primary

TABLE I
TRANSFORMER DESIGN PARAMETERS

$N_1 : N_2$	R (Ω)	L_μ (μH)	K
1:100	10	2	100

TABLE II
TRANSFORMER DESIGN PARAMETERS

I_{dc} (A)	i_{ac} (mA)	W_m (μJ)	Minimum V_c (mm^3)	Core Dim. (OD/ID/HT) (mm)	Actual L_μ (μH)
1	100	0.5	22.79	5.8/3.1/1.5	3.276
10	100	50	2279	22/14/13	2.080
20	100	200	9118	39/20/13	3.014
50	100	1250	56990	102/66/15	2.314

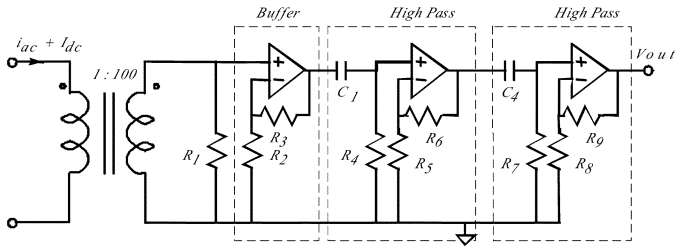

Fig. 3. Schematic of the prototype current-transformer sensor. $R_1 = 10\,\Omega, R_2 = R_5 = R_8 = 220\,\Omega, R_3 = R_6 = R_9 = 820\,\Omega, R_4 = R_7 = 1\,\text{k}\Omega, C_1 = C_2 = 0.2\,\mu\text{F}$.

side. A minimum magnetizing inductance of 2 :H results in a low-frequency cutoff of approximately 80 Hz, over two decades below the fundamental. To achieve the desired overall sensor gain, an amplifier gain of 100 is selected.

Ferrite core material 3F3 is selected for the transformer design. This material has a permeability of 1800 μ_o, a maximum flux density of 450 mT, and has low core loss for frequencies below about 700 kHz. Table II shows the transformer design parameters for different dc current levels. As can be seen, the dimensions of the core rise rapidly with increasing dc current rating.

A CT sensor based on these design parameters has been prototyped and tested. A schematic of the sensor, which has a dc current rating of 20 A, is shown in Fig. 3. To achieve the required gain of 100 with low phase shift for the frequencies of interest, a three-stage amplifier based on an LT1230 quad current-feedback op amp is used. Each stage has a gain of approximately 4.7, and the second and third stages are ac coupled so that only ripple-frequency components are amplified; ac coupling is not necessary in the first stage due to the action of the current transformer. Dividing the total required gain equally in the fashion selected achieves the lowest phase shift in the output signal.

Fig. 4 shows experimental results from the sensor; the bottom trace is the sensor input current, while the top trace is the sensor output voltage. This plot demonstrates that the sensor accurately measures the high-frequency ripple current; similar results are obtained with dc current bias levels up to the dc current rating of the sensor. Measurements with a network analyzer confirm that the sensor has accurate gain and phase (within 5°) up to approximately 1 Mhz (Fig. 5). One may thus conclude that the

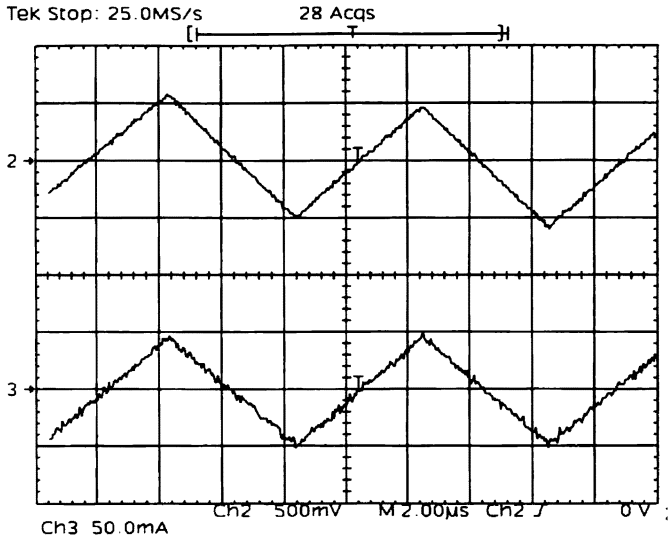

Fig. 4. Output waveform of the current-transformer sensor (top waveform, Ch 2, 500 mV/div) as compared to the input current measured by a current probe (bottom waveform, Ch 3, 50 mA/div). The horizontal scale is 2 μS/div.

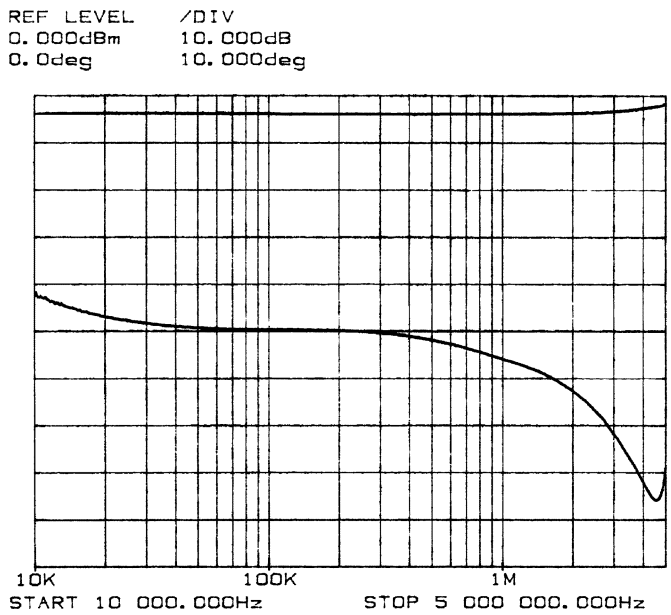

Fig. 5. Spectral performance of the current transformer sensor.

current transformer sensor is an effective approach for this application. However, the sensor is better suited to low-current applications than to high-current applications as the CT core size grows quadratically with dc current level.

C. Rogowski Coil Sensor

A current sensing approach that has not been previously employed in this application is the use of a Rogowski coil [14]–[16]. The Rogowski sensing technique has been known since 1912 [14], but has typically been used to sense large currents [15], [16] because of the low gain of the coil. Nevertheless, through proper design we have been able to adapt this technique to the small ripple current magnitudes found in

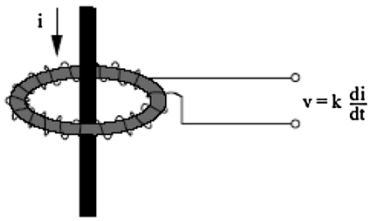

Fig. 6. Rogowski coil. The sense coil is a uniform single-layer winding on an air-core former.

active ripple filter applications. Here we address the design of Rogowski-coil sensors for this application [17].

The Rogowski coil itself comprises a uniform single-layer winding on a nonmagnetic toroidal core (Fig. 6). The open-circuit voltage induced on the winding is proportional to the derivative of the current passing through the toroid

$$v = \frac{\mu_0 N A_t}{l_c}\frac{di}{dt} = k\frac{di}{dt} \tag{3}$$

where N is the number of winding turns, A_t the cross-sectional area of the toroid, and l_c is the mean path length around the toroid. An integrating amplifier stage is then used to convert this signal into an output voltage that is proportional to the input current waveform. This sensing technique has a number of advantages which make it well-suited to this application: it is accurate and has very high bandwidth, yields an isolated output signal and does not load the circuit, it is insensitive to system parameter variations and does not suffer from dc-current saturation effects, and is relatively simple and inexpensive to manufacture.

The design of the coil is governed by a number of factors. Given a maximum practical ratio of the toroid cross section to circumference (A_t/l_c), the only methods to increase the gain of the coil are to increase its size (both A_t and l_c in proportion), or to increase the number of turns on the coil, or to increase the number of times the current to be sensed is passed through the toroid. The size of the coil and the number of times the current to be sensed is passed through it are limited by the desire to have a compact, inexpensive sensor. Increasing the number of turns on the coil increases the output inductance of the coil, which limits the high-frequency performance of the sensor. To understand this, consider that a basic Thévenin model for the coil is the induced voltage (from the sensed current) in series with the coil inductance. To keep the high-frequency impedance at the coil output node low (for converter noise rejection) and to prevent the coil inductance from resonating with the amplifier input, the coil needs to be terminated with a sufficiently low resistance (typically in the kΩ range) by the amplifier. The output inductance of the coil forms a low-pass filter with the amplifier input impedance, affecting the phase (and eventually the magnitude) of the amplified signal. Thus, to achieve good high-frequency performance, there is a limit on the acceptable coil output inductance, and hence on the number of coil turns used.

In the prototype Rogowski coil developed to validate this new approach, these factors were traded off against one another, resulting in good sensing gain and bandwidth for ripple currents at the 100-mA level in the 100+ kHz range. The toroid (i.d. = 18 mm, o.d. = 32 mm, height = 13 mm), was wound with 88 turns of 31-gauge wire, and the current to be sensed was passed through the coil five times, yielding a total gain k of 6.4H10^{-7} V-s/A. The 14 μH output inductance of the coil was terminated with an amplifier input resistance of 1 kΩ, yielding acceptable bandwidth and damping.

To adapt the Rogowski sensing technique to the low ripple current levels encountered in active filtering applications, a four-stage amplifier based on a single LT1230 quad current-feedback op amp IC was developed (Fig. 7). The amplifier performs the necessary frequency shaping and amplification for ripple-frequency components, while rejecting low-frequency components. The amplifier is composed of four stages: a gain stage and two high-pass/gain stages, each with a pass-band gain of 4.7, and a ripple-frequency integrator stage. The integrator stage acts as a differentiator (gain increasing 20 dB/decade) for frequencies below 1 kHz, and acts as an integrator (gain decreasing 20 dB/decade) for higher frequencies (with a gain of 0.16 at 100 kHz). To meet the high-gain, high-bandwidth requirements of the system with small phase shift at the frequencies of interest, current feedback op amps are used. The op amps are configured as noninverting (fixed gain) amplifiers, and are used along with passive elements to achieve the necessary filtering and amplification. With this four-stage amplifier, the current sensor has a mid-band gain of 6.6 V/A, and a useful (low phase-shift) bandwidth of approximately 1 MHz (Fig. 8). Fig. 9 shows experimental results from the prototype sensor.

D. Current Sensor Comparison

The Rogowski-coil sensor is approximately the same size and has similar levels of complexity and performance as the 20 A current transformer sensor (though it is significantly lighter owing to its use of a nonmagnetic core). Because the size of the Rogowski-coil sensor is invariant to the dc current level in the system while the size of the current transformer grows quadratically with it, one may conclude that for low-current systems the CT sensor is more advantageous, while for high-current systems the proposed Rogowski-coil sensor is better. For the design parameters considered here, this crossover is in the vicinity of 20 A or lower.

III. Current Injection

The second major active filter element is the current injector. The current injector is designed to inject an exact replica of the sensed current (with opposite polarity) at the output of the active filter, thus canceling the sensed ripple current. As with the current sensor, it must have high accuracy, wide bandwidth, and a small phase shift in order to be effective. To achieve the required performance, the current injector is typically implemented with linear amplifier circuits, making it a dissipative element. Nevertheless, it should be pointed out that while the injected ripple currents may be large, the power injected into the output may actually be very small, because the ripple voltage seen at the injection point may be quite small. An ideal injector would thus only inject an ac current into the output while only overcoming a small ac voltage ripple to do so, thus achieving low dissipation.

A. Class A Current Injector

One approach, illustrated in Fig. 10, is the use of an injector with a class A output stage [9], [11]. This approach has the advantage of extreme simplicity, and accurate, high-bandwidth current injection is easily achieved. The primary limitation of

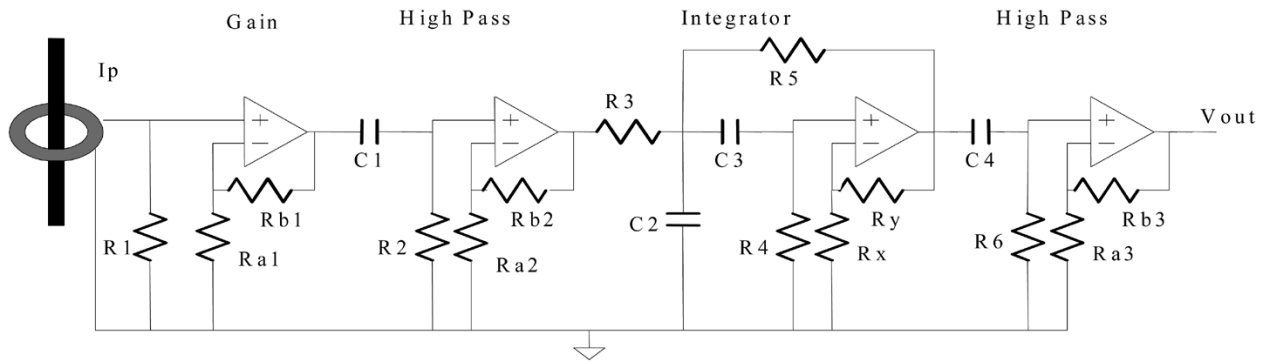

Fig. 7. Amplifier for the Rogowski-coil current sensor. The circuit is based on an LT1230 quad current-feedback amplifier. $R_{a1} = R_{a2} = R_{a3} = 220\ \Omega$, $R_{b1} = R_{b2} = R_{b3} = 820\ \Omega$, $R_1 = R_2 = R_6 = 1\ \text{k}\Omega$, $R_3 = R_4 = 750\ \Omega$, $R_5 = 4.3\ \text{k}\Omega$, $R_x = 200\ \Omega$, $R_y = 4.2\ \text{k}\Omega$.

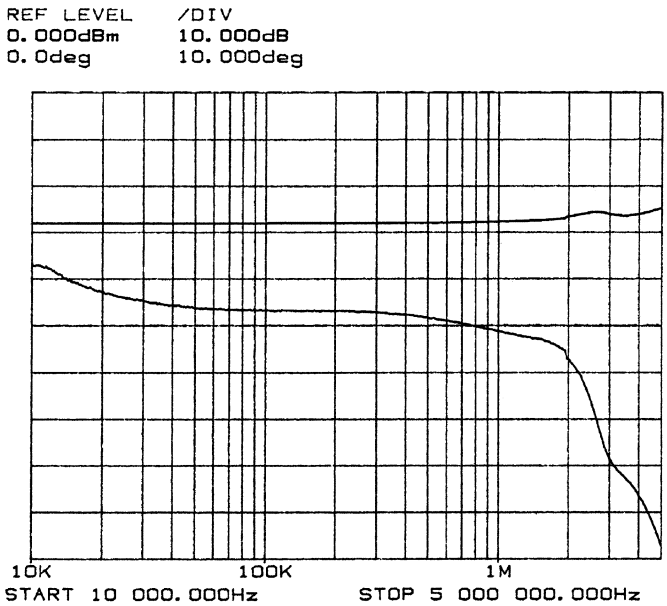

Fig. 8. Spectral performance of the Rogowski Coil sensor.

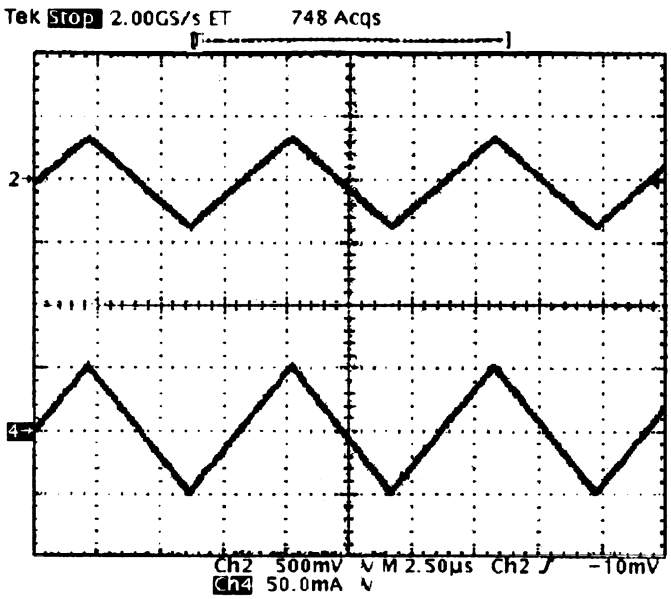

Fig. 9. Output waveform of the Rogowski-coil sensor (top waveform, Ch 2, 500 mV/div) as compared to the input current measured by a current probe (bottom waveform, Ch 4, 50 mA/div). The horizontal scale is 2.5 μS/div.

this current injector is efficiency. The class A circuit is characterized by the fact that the output transistor conducts continuously and so must carry a dc bias current greater than the peak magnitude of the ac injection current. The ac injection current is drawn from the low-impedance injection node via a coupling capacitor, while the dc bias current is supplied from a voltage source via a resistor. (If the injection node voltage is sufficiently low, the bias current may be drawn from there, as in Fig. 10.) The dissipation associated with the bias current is substantially greater than the dissipation associated with the ac current, and is typically the limiting factor in the achievable ac injection current magnitude.

Fig. 11 shows a circuit of the type shown in Fig. 10 that is designed to inject ac currents of up to 100 mA into the 14 V output node of a 230 W, 125 kHz power converter. An LM6361 op amp is used along with a ZTX 649 transistor to achieve a wide injection bandwidth with low phase shift. Additional passive elements are used for current limiting and for protecting the injector during transients. The 125-mA bias current is drawn directly from the 14-V injection node, resulting in 1.75 W of dissipation. Nevertheless, this represents less than 1% of converter output power and is thus deemed acceptable.

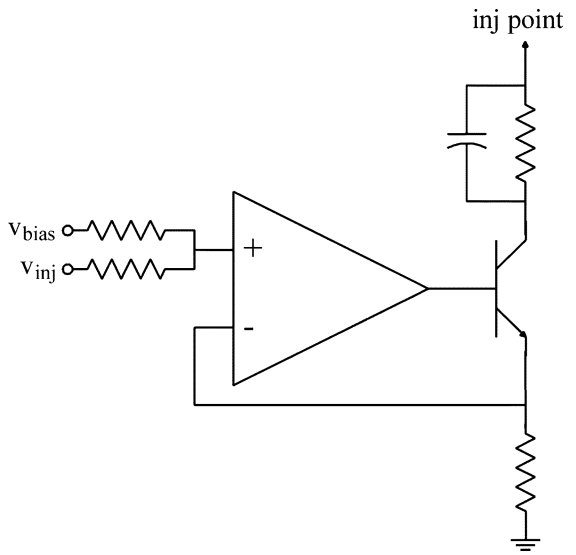

Fig. 10. Structure of one class A current injection circuit.

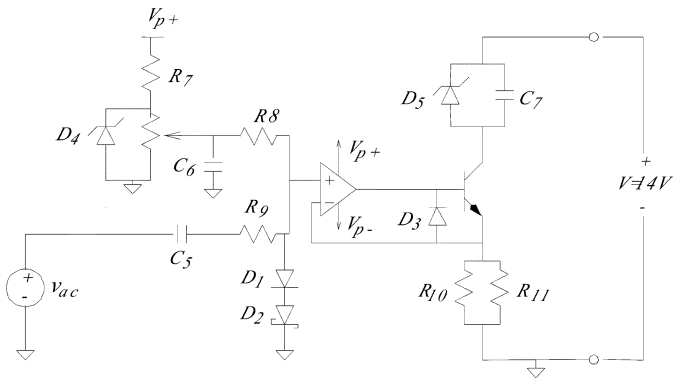

Fig. 11. Schematic of a class A injector circuit using an LM6361 op amp and a ZTX649 transistor. $R_7 = R_8 = R_9 = 1$ kΩ, $R_{10} = 3.3\ \Omega$, $R_{11} = 50\ \Omega$, $C_5 = C_6 = C_7 = 0.1\ \mu$F, D_1 (1N4143), D_2 (BYV10-40), D_3 (1N4148), D_4 (BZX85C5V1), D_5 (BZX85C6V8).

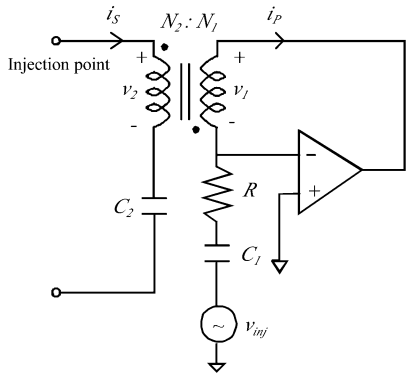

Fig. 12. Structure of a transformer-based current injector.

B. Transformer-Coupled Current Injector

While the class A injector is simple, accurate, and wide bandwidth, the bias current dissipation severely limits the achievable injection current magnitude. An alternative approach is the use of a linear amplifier with a class B or AB output stage that does not impose this constraint. Introduction of a current transformer and coupling capacitor (as illustrated in Fig. 12) simplifies the injector electronics and allows large injected current magnitudes to be achieved [5], [8]. The coupling capacitor C_2 blocks the dc voltage at the injection node so the transformer and injector amplifier see only ac voltages. The transformer converts the relatively high-voltage, low-current output of the linear amplifier to the low-voltage, high-current signal required at the injection node. The resistor R and transformer turns ratio set the voltage-to-current gain of the injector, while the blocking capacitor C_1 is merely present to ac-couple the injection command to the injector.

A major advantage of this injector approach is low power dissipation, since the amplifier only needs to drive an ac current into an ac voltage. Injection levels of as much as an amp have been achieved without undue dissipation using this method [8]. The drawbacks to this approach are the cost and volume of the current transformer and coupling capacitor, and the performance limitations introduced by their parasitics. Here we present the design and evaluation of a transformer-based current injector circuit.

Design of an injector circuit of the type shown in Fig. 12 starts with a specification of the necessary voltage and current

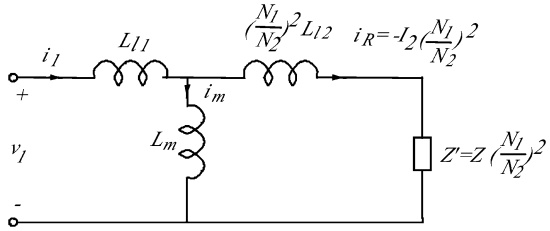

Fig. 13. Model for the impedance seen looking from the primary (amplifier) side of the injector transformer into the secondary side.

ripple magnitudes at the injection node. The product of the peak voltage and current limits of the injector amplifier $(V_{\rm pk}, I_{\rm pk})$ must be greater than the product of the ripple voltage and ripple current at the injection node. The transformer turns ratio is selected to match the voltage and current swing of the amplifier to that needed at the injection node. The transformer is designed with a nongapped high permeability core. Fig. 13 shows one model for the impedance seen from the primary (amplifier) side of the transformer, including the transformer parasitics and the reflected secondary-side impedance. To achieve the desired current injection accuracy, the current used to magnetize the transformer core (i.e., the magnetizing current i_μ) must be only a very small percentage of the total amplifier current (e.g., 1%). Given a maximum injection current and voltage and transformer turns ratio, this imposes a lower bound on the transformer magnetizing inductance L_μ seen from the primary side. Neglecting transformer leakage, this requirement can be expressed as

$$L_\mu \geq \frac{\lambda_{\rm pk}}{i_{\mu,\max}}. \tag{4}$$

In this equation, $\lambda_{\rm pk}$ is the peak flux linkage, calculated as the maximum of the time integral of the injector amplifier output voltage. For a sine-wave voltage, $\lambda_{\rm pk}$ may be calculated as

$$\lambda_{\rm pk} = \frac{V_{\rm pk}}{\pi f_{\rm sw}} \tag{5}$$

while for a worst-case square-wave ripple voltage, this becomes

$$\lambda_{\rm pk} = \frac{V_{\rm pk}}{2 f_{\rm sw}}. \tag{6}$$

Based on the desired turns ratio and the required primary-side magnetizing inductance, the injector transformer may be designed. The minimum number of primary (amplifier) side turns needed for the transformer may be expressed as

$$N_1 = \sqrt{\frac{L_\mu l_c}{\mu A_c}} \tag{7}$$

where l_c is the effective core magnetic path length, A_c is the effective core cross section, and is the core permeability. The number of primary turns selected may need to be adjusted in order to ensure an integer number of turns on the secondary. The core cross section required to prevent saturation is

$$A_c > \frac{\lambda_{\rm pk}}{N_1 B_{\rm sat}} \tag{8}$$

where $B_{\rm sat}$ is the saturation flux density of the core material. Finally, the core should have sufficient winding space to accept the primary and secondary windings. One may start by selecting an approximate number of turns using an estimated ratio of l_c

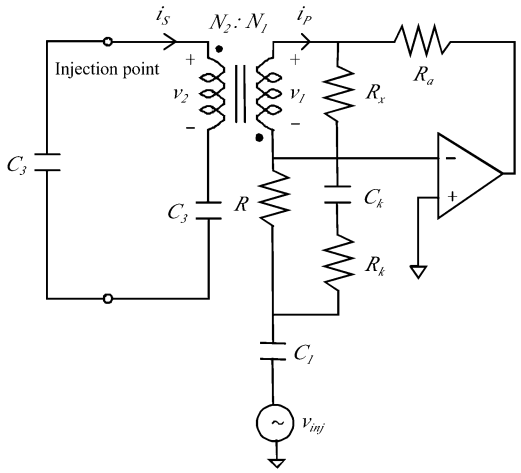

Fig. 14. Schematic of a transformer-based injector circuit using an LM6361 op amp. $R = R_{\rm k} = 160\ \Omega, R_{\rm x} = 3.9\ {\rm k}\Omega, R_{\rm b} = 100\ \Omega, C_1 = 1\ \mu$F, $C_2 = 50\ \mu$F, $C_3 = 20\ \mu$F, $C_{\rm k} = 1$ nF.

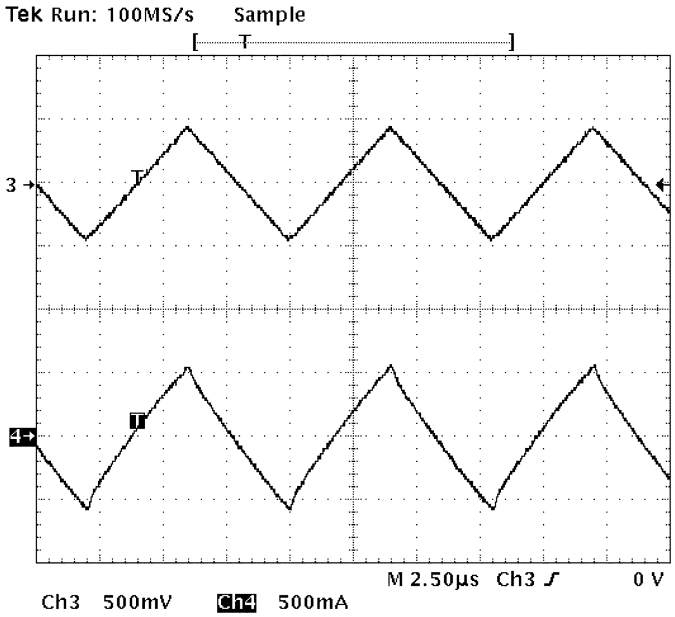

Fig. 15. Input command to the transformer-based injector (top waveform, Ch 3, 500 mV/div) as compared to the injected current as measured by a current probe (bottom waveform, Ch 4, 500 mA/div). The horizontal scale is 2.5 μS/div. The phase shift of the injected current with respect to the command is less than 4° at the fundamental frequency of 125 kHz.

to A_c. (The ratio of l_c to A_c falls into a rather narrow range of values for typical cores of a given size.) A core satisfying the cross-sectional area requirement may then be selected, and verified to have sufficient winding room. The calculation of turns may then be refined based on the exact core, and the core area and winding area constraints rechecked.

Based on these considerations, a prototype transformer injector circuit capable of 1 A injection current at low loss was developed and tested. The schematic for the circuit is shown in Fig. 14. The impedance looking into the output of the power converter is modeled as a capacitor (C_3). There are a few additional passive components in this figure as compared to Fig. 12; these elements are to compensate the op amp. A 50:2 turns ratio on a Philips TX 22/14/13 3F3 ferrite core was selected for the transformer. This results in a peak op-amp current of 40 mA, with less than 1% magnetizing current error.

Fig. 15 shows experimental results from the transformer-based injector. Channel 3 displays the 125-kHz injection command, while Channel 4 shows the injected current. The injected current has an accurate gain with a phase shift of less than 4° at the fundamental (switching) frequency.

IV. Application to a Power Converter

Here we describe the application of active ripple filtering to the output filter of a dc/dc converter. The active filter comprises the novel Rogowski-coil current sensor described in Section IIC and the class A current injector of Section IIIA. This active filter is coupled with a small passive filter to form a hybrid passive/active filter. The proposed technique has been applied to the output filter of a 230 W, 12- kHz buck converter with a 42-V nominal input voltage and a 14-V nominal output voltage (Fig. 1). The discontinuous-mode converter uses a 1.4 μH buck inductor and a 20 μF primary output capacitor. The converter operates under averaged current-mode control, and regulates the voltage at the inside of the EMI filter such that the filter dynamics do not appear inside the converter's voltage control loop. A more detailed view of the output filter elements can be found in Fig. 16, which shows the experimental setup used to test the new approach. The passive filter element values used in the hybrid passive/active filter are $L_1 = 9\ \mu$H, $C_1 = 5\ \mu$F, $L_2 = 51\ \mu$H,

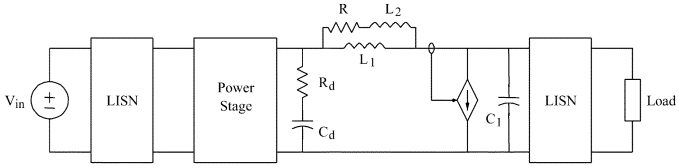

Fig. 16. Experimental setup used to test the new active filtering method.

$R = 0.56\ \Omega, C_d = 47\ \mu$F, $R_d = 3.3\ \Omega$. The size of the filter inductors L_1 and L_2 are such that they carry a total of approximately 100 mA of ripple current[2]. The active filter is designed to cancel this ripple current.

It should be pointed out that despite the term "feedforward" active filter, the active element *does* affect the dynamics of the hybrid passive/active filter. This is because the current being canceled is not an independent input, but is in fact a function of the output voltage, which is in turn affected by the injected current. Nevertheless, starting with a transfer function from sensed to injected current, the dynamics of the hybrid filter system are easily determined. In the case studied here, the addition of the active element reduces the filter damping; the introduction of the small RC damping leg in the filter was in response to this effect.

Tests of the active filter circuit were conducted with the experimental setup shown in Fig. 16, using conventional EMI test methods. Experiments were carried out over a ground plane, and 50 Ω line impedance stabilization networks (LISNs) were employed to provide controlled ripple-frequency impedances at the input and output of the system under test. (A LISN is a filter which passes power-frequency currents, but which shunts

[2]This is a reasonable intermediate current specification, as the filter reduces the large ripple injected through the buck inductor (>10 A) down to the small ripple current allowed into the LISN (<100 μA). The 100-mA ripple in the filter inductor is in the vicinity of the geometric mean of these extremes.

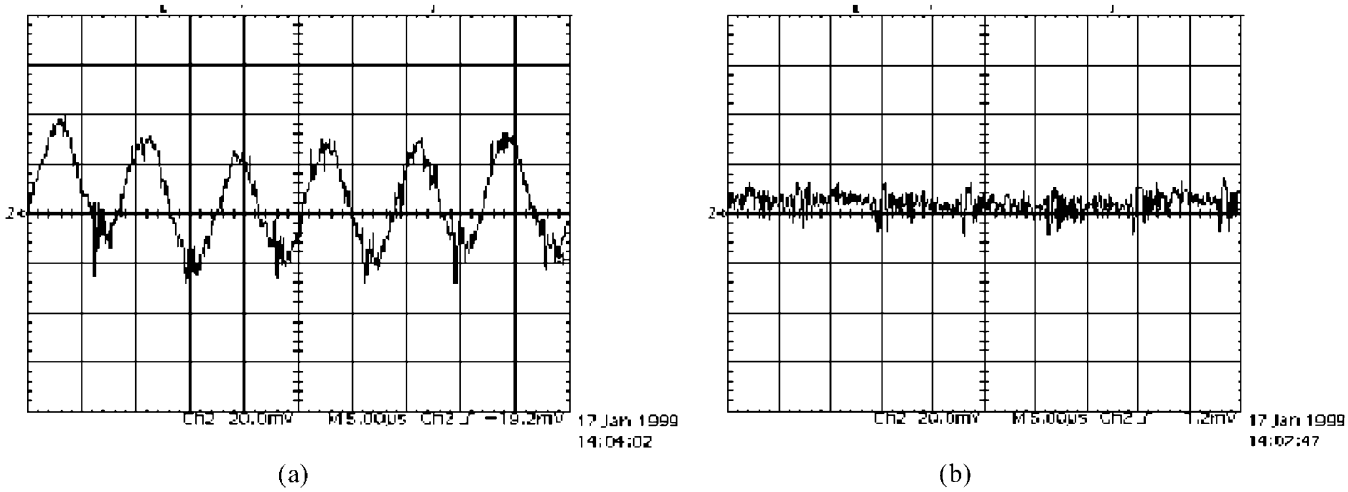

Fig. 17. LISN output voltage for converter with hybrid passive/active output filter operating at a 1-Ω load. In each case the vertical scale is 20 mV/div, and the horizontal scale is 5 μS/div. (a) Only the passive portion of the hybrid filter (without active cancellation). (b) Full hybrid filter (with active cancellation).

ripple frequency currents into a known impedance.) The LISN ripple voltage (the standard metric in conducted EMI specifications) was used to evaluate filter effectiveness; this is equivalent to measuring the current into the known ripple-frequency impedance of the LISN. Except as noted, all experimental results have been obtained with a 1-Ω resistive load.

The following test procedure was used. First, measurements were made using only the passive portion of the hybrid passive/active filter. Next, the active filter portion was added in, and a second set of measurements was taken. Finally, an entirely passive filter was designed which allows the converter to meet the same ripple specification as with the hybrid passive/active filter, and a final set of measurements was taken using this entirely passive filter.

A. Hybrid Passive/Active Filter

Fig. 17(a) shows the LISN voltage using only the passive portion of the hybrid filter, while Fig. 17(b) shows the LISN voltage with the active element of the hybrid filter included. There is clearly a substantial reduction in the switching ripple when the active filter element is employed. Fig. 18 shows the spectrum of the LISN voltage both with and without the use of the active filter element. A reduction of over 30 dB is achieved in the fundamental ripple component through use of the active filter. Note that significant reductions are not achieved at higher frequencies. This is not because the active filter does not have enough bandwidth; rather, these components are so small that they are at the noise and pickup floor of the prototype active filter, and hence cannot be effectively eliminated by it. Nevertheless, through use of the active filter element, the converter is able to meet a ripple specification that is flat across frequency (63 dB μV), which it would not meet using only the passive portion of the filter.

B. Comparison to an Equivalent Passive Filter

In order to provide a fair assessment of the advantages of the proposed active filter method, an entirely passive filter was designed which allows the converter to meet the same flat ripple specification across frequency as with the hybrid filter. The passive filter was constructed using the same filter topology as the passive portion of the hybrid filter. Referring to Fig. 16, the component values for the entirely passive filter were selected as $L_1 = 225$ μH, $C_1 = 5$ μF, $L_2 = 576$ μH, $R = 1.9\ \Omega$, $C_d = 47$ μF, $R_d = 3.3\ \Omega$. Fig. 19 shows the spectrum of the LISN voltage for both the hybrid filter and the entirely passive filter. Each filter allows the converter to meet the same flat ripple specification (63 dB μV). At higher frequencies, the entirely passive filter provides more attenuation than the hybrid filter. This

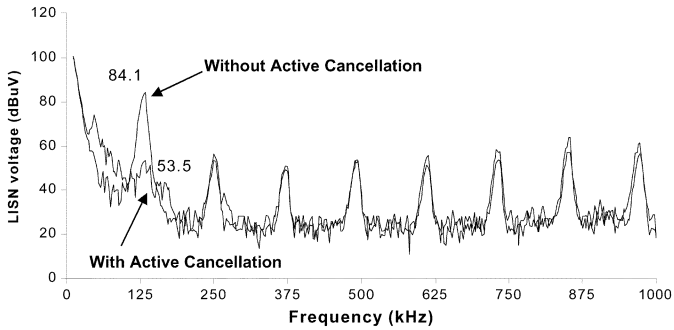

Fig. 18. LISN output voltage spectra for converter operation with the hybrid passive/active filter. Plots are shown for operation both with and without active cancellation. Use of active cancellation results in more than a 30-dB reduction in the fundamental ripple voltage.

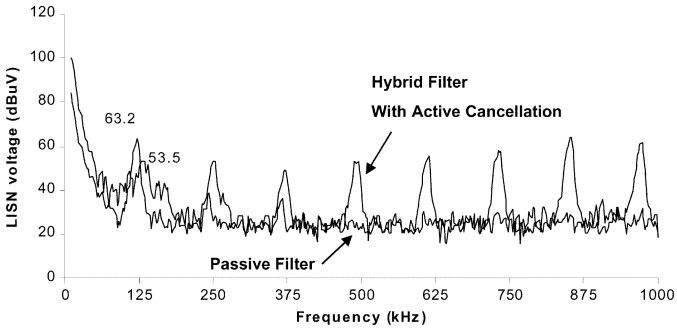

Fig. 19. LISN output voltage spectra for converter operation with two different filters. Plots are shown for operation with the hybrid passive/active filter, and also with an entirely passive filter. The two filters meet the same flat ripple specification ($\sim$ 63 dB:V), but the hybrid filter is substantially smaller.

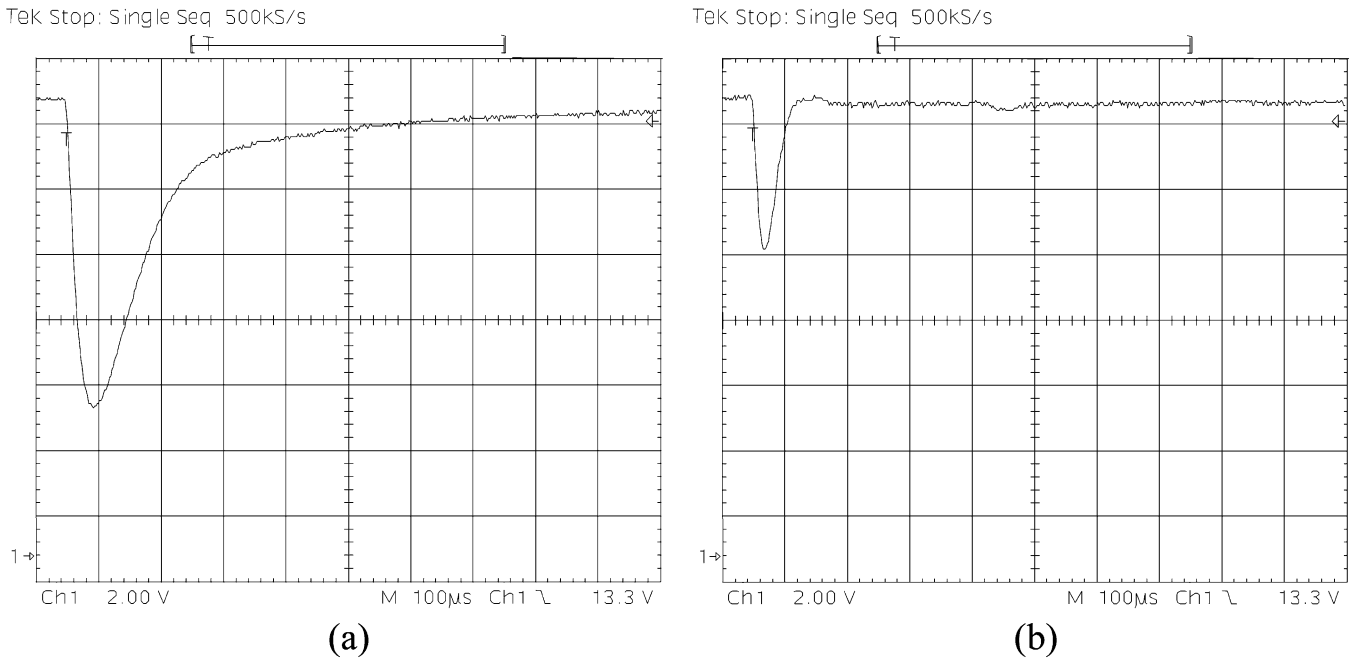

Fig. 20. Output voltage transient response of the converter for a load step from 3 Ω to 1.5 Ω. (a) Response using entirely passive filter. (b) Response with hybrid passive/active filter. In each case, the vertical scale is 2 V/div, and the horizontal scale is 100 μS/div. The transient magnitude and duration are far smaller with the hybrid filter.

is essentially because it had to be overdesigned for high frequencies in order to meet the ripple specification at the fundamental (which is the hardest component to attenuate with a passive filter). The important result, however, is the relative size of the two filters: the weight of the hybrid filter is only 20% of that of the passive filter. Thus, through use of the active filtering technique a factor of 5 reduction in overall filter mass has been achieved. One penalty of the active approach is in efficiency. The active filter dissipates approximately 1.8 W (mainly due to the injector), whereas the loss in the passive filter is more than an order of magnitude lower. This corresponds to an approximate efficiency penalty of 0.8% at full load for the active approach (see Fig. 20).

A second advantage of the active filtering approach is in the transient performance of the system. Because a hybrid passive/active filter can employ smaller passive (energy storage) components than an entirely passive filter, it is expected that one can achieve faster dynamic control of the output when active filtering techniques are used. (Note that because the active filtering circuitry can only inject small-signal currents, it has very little effect during large-signal transients.) To investigate this, the output voltage response to load transients was measured both with the hybrid filter and with the entirely passive filter. (The LISNs were not employed during these tests, as only the low-frequency transient response was of interest.) Fig. 19(a) shows the output voltage response of the system to a load step from 3 Ω to 1.5 Ω using the entirely passive filter, while Fig. 19(b) shows the response to the same load step using the hybrid filter. Both the magnitude and duration of the output voltage transient are substantially smaller when the hybrid filter is used, demonstrating the advantages in transient performance that can be obtained using the active filtering approach.

V. Conclusion

An active ripple filter is an electronic circuit that cancels or suppresses the ripple current and EMI generated by the power stage of a power converter, thus reducing the passive filtration requirements. This paper explores the design of active ripple filters that operate through feedforward cancellation of converter or filter ripple currents. Design of both the current sensor and current injector elements of these filters is considered, and the advantages, limitations, design tradeoffs, and experimental performance of a variety of different implementation methods are addressed.

The design and performance of an active filter incorporating a novel Rogowski-coil current sensor is discussed in detail. Experimental results from a prototype converter system using this approach are presented, and quantitative comparisons are made between a hybrid passive/active filter and a purely passive filter. It is demonstrated that substantial improvements in filter mass and converter transient performance are achievable using this active ripple filtering method. It may be concluded that use of active techniques such as those described here can provide significant benefits in power conversion applications.

References

[1] T. K. Phelps and W. S. Tate, "Optimizing passive input filter design," in *Proc. Powercon 6*, May 1979, pp. G1-1–G1-10.

[2] M. J. Nave, *Power Line Filter Design for Switched-Mode Power Supplies*. New York: Van Nostrand Reinhold, 1991.

[3] D. M. Mitchell, "Power line filter design considerations for dc-dc converters," *IEEE Ind. Applicat. Mag.*, vol. 5, no. 6, pp. 16–26, Nov./Dec. 1999.

[4] S. Y. M. Feng, W. A. Sandler, and T. G. Wilson, "Small-capacitance nondissipative ripple filters for DC supplies," *IEEE Trans. Magn.*, vol. MAG-6, no. 1, pp. 137–142, Mar. 1979.

[5] J. Walker, "Design of practical and effective active EMI filters," in *Proc. Poweron 11*, vol. I-3, 1984, pp. 1–8.
[6] L. E. LaWhite and M. F. Schlecht, "Active filters for 1-MHz power circuits with strict input/output ripple requirements," *IEEE Trans. Power Electron.*, vol. PE-2, no. 4, pp. 282–290, Oct. 1987.
[7] T. Farkas and M. F. Schlecht, "Viability of active EMI filters for utility applications," *IEEE Trans. Power Electron.*, vol. 9, no. 3, pp. 328–337, May 1994.
[8] P. Midya and P. T. Krein, "Feed-forward active filter for output ripple cancellation," *Int. J. Electron.*, vol. 77, no. 5, pp. 805–818, 1994.
[9] D. C. Hamill, "An efficient active ripple filter for use in DC-DC conversion," *IEEE Trans. Aero. Electron. Syst.*, vol. 32, no. 3, pp. 1077–1084, Jul. 1996.
[10] M. S. Moon and B. H. Cho, "Novel active ripple filter for the solar array shunt switching unit," *J. Propulsion Power*, vol. 12, no. 1, pp. 78–82, Jan./Feb. 1996.
[11] M. T. Thompson and M. F. Schlecht, "High power laser diode driver based on power converter technology," *IEEE Trans. Power Electron.*, vol. 12, no. 1, pp. 46–52, Jan. 1997.
[12] N. K. Poon, J. C. P. Liu, C. K. Tse, and M. H. Pong, "Techniques for input ripple current cancellation: Classification and implementation," *IEEE Trans. Power Electron.*, vol. 15, no. 6, pp. 1144–1152, Nov. 2000.
[13] A. C. Chow and D. J. Perreault, "Design and evaluation of a hybrid passive/active ripple filter with voltage injection," *IEEE Trans. Aerosp. Electron. Syst.*, vol. 39, no. 2, pp. 471–480, Apr. 2003.
[14] W. Rogowski and W. Steinhaus, "Die Messung der Magnetischen Spannung," *Arch. Electrotech.*, vol. 1, 1912.
[15] W. F. Ray and R. M. Davis, "Wide bandwidth Rogowski current transducers, part 1: The Rogowski coil," *EPE J.*, vol. 3, no. 1, pp. 51–59, Mar. 1993.
[16] A. Radun, "An alternative low-cost current-sensing scheme for high-current power electronics circuits," *IEEE Trans. Ind. Electron.*, vol. 42, no. 1, pp. 78–84, Feb. 1995.
[17] M. Zhu, D. J. Perreault, V. Caliskan, T. C. Neugebauer, S. Guttowski, and J. G. Kassakian, "Design and evaluation of an active ripple filter with Rogowski-coil current sensing," in *Proc. IEEE Power Electronics Specialists Conf.*, 1999, pp. 874–880.

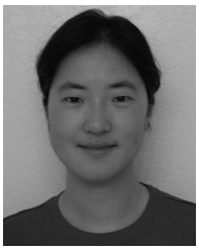

Mingjuan Zhu was born in HanDan, China, on September 30, 1975. She received the B.S. and M.Eng. degrees in electrical engineering from the Massachusetts Institute of Technology, Cambridge, in 1999.

In 1999, she joined Lucent Technologies, Holmdel, NJ, where she was involved with EDFA control circuit design. In 2000, she joined Agilent Technologies, Santa Rosa, CA, where she worked on low phase noise crystal oscillator design and frequency reference circuits. Since July 2003, she has been with Remec, Inc., San Diego, CA, where she is currently working on Ka band transceiver design.

David J. Perreault (S'91–M'97) received the B.S. degree from Boston University, Boston, MA, in 1989, and the S.M. and Ph.D. degrees from the Massachusetts Institute of Technology (MIT), Cambridge, in 1991 and 1997, respectively.

In 1997 he joined the MIT Laboratory for Electromagnetic and Electronic Systems as a Postdoctoral Associate, and became a Research Scientist in the laboratory in 1999. In July of 2001, he joined the MIT Department of Electrical Engineering and Computer Science, where he is presently the Emanuel E. Landsman Associate Professor of Electrical Engineering. His research interests include design, manufacturing, and control techniques for power electronic systems and components, and in their use in a wide range of applications.

Dr. Perreault received the Richard M. Bass Outstanding Young Power Electronics Engineer Award from the IEEE Power Electronics Society, the ONR Young Investigator Award, and two IEEE prize paper awards. He is a Member of Tau Beta Pi and Sigma Xi.

Vahe Caliskan received the B.S. (with honors) and M.S. degrees from the University of Illinois, Chicago, in 1990 and 1993, respectively, and the Sc.D. degree from the Massachusetts Institute of Technology (MIT), Cambridge, in 2000.

At the University of Illinois (1990–1994), he was a Research Assistant at the Power Electronics Research Laboratory and a Teaching Assistant in the EECS Department. At MIT (1994–2000), he was a Research Assistant in the Laboratory for Electromagnetic and Electronic Systems where he was involved in the development of dual-voltage automotive electrical power systems. In November 2000, he joined Motorola, Inc., where he is presently a Principal Staff Engineer in the Automotive Communications and Electronic Systems Group. His research interests include power electronics, automotive electrical/electronic systems, analog circuit design, and computer-aided modeling/simulation.

Dr. Caliskan received the Outstanding Teaching Assistant Award in 1993. He is a Member of Tau Beta Pi, Eta Kappa Nu, and Sigma Xi.

Timothy C. Neugebauer received the B.S. degree in electrical engineering from Union College, Schenectady, NY, in 1997 and the S.M. and Ph.D. degree from the Massachusetts Institute of Technology (MIT), Cambridge, in 1999 and 2004.

From 1997 to 2004, he was a graduate student in the LEES Laboratory, MIT. At MIT, he worked in the areas of dc/dc converters, multi-level inverters, and the design of passive elements. He is currently working at Draper Laboratories, Boston, MA.

Stephan Guttowski was born in Berlin, Germany, in 1969. He received the M.S. and Ph.D. degrees from the Technical University Berlin, Berlin, Germany, in 1994 and 1998, respectively, both in electrical engineering. His doctoral thesis contained the investigation of the electromagnetic compatibility (EMC) of power electronic systems.

From 1998 to 1999, he was a Post-Doctoral Researcher in the Laboratory for Electromagnetic and Electronic Systems, Massachusetts Institute of Technology (MIT), Cambridge. In 1999, he joined DaimlerChrysler Corporate Research, Berlin, Germany, where he continues to explore the EMC aspects of power electronic systems in electric drives. In 2001, he joined the Fraunhofer Institute for Microintegration and Reliability (IZM), Berlin, Germany, where he has established a research group in the field of power electronic system integration. His main research area is the aspects of electromagnetic reliability of power electronic systems.

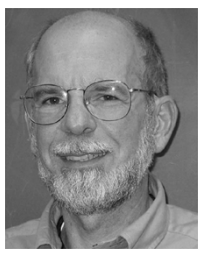

John G. Kassakian (F'89) received the B.S., M.S., and Ph.D. degrees from the Massachusetts Institute of Technology (MIT), Cambridge.

He is Director of the Laboratory for Electromagnetic and Electronic Systems, MIT, and prior to joining the MIT faculty, served a tour of duty in the U.S. Navy. He has published extensively in the areas of power electronics, education, and automotive electrical systems, and is coauthor of the *Principles of Power Electronics*.

Dr. Kassakian received the IEEE Centennial Medal, the IEEE William E. Newell Award, the IEEE Power Electronics Society's Distinguished Service Award, and the IEEE Millennium Medal. He is a Member of the National Academy of Engineering and is the Founding President of the IEEE Power Electronics Society.